

Stress release and defect occurrence in $V_{1-x}Fe_x$ films upon hydrogen loading: H-induced superabundant vacancies, movement and creation of dislocations

R. Gemma^{a,d,*}, P. Dobron^b, J. Cizek^c, A. Pundt^{a,*}

^a Institute of Material Physics, University of Göttingen, Friedrich-Hund-Platz 1, D-37077 Göttingen, Germany

^b Department of Physics of Materials, Faculty of Mathematics and Physics, Charles University in Prague, Ke Karlovu 5, 12116 Prague 2, Czech Republic

^c Department of Low Temperature Physics, Faculty of Mathematics and Physics, Charles University in Prague, V Holesovickach 2, Prague 8, Czech Republic

^d Physical Sciences and Engineering Division, King Abdullah University of Science and Technology (KAUST), Thuwal 23955-6900, Saudi Arabia

Received 13 June 2013; received in revised form 21 December 2013; accepted 22 December 2013

Abstract

Hydrogen-induced elastic/plastic deformation was studied in $V_{1-x}Fe_x$ ($x = 0.02\text{--}0.08$) films with thicknesses between 10 and 400 nm and prepared at different temperatures. The combination of several in situ techniques such as X-ray diffraction, acoustic emission, electromotive force and substrate curvature techniques allows sensitive studies of defects generated in these thin films. As well as conventional out-of-plane linear elastic film expansion and in-plane compressive stress increase during hydrogen absorption, the investigations uncovered new details: as soon as hydrogen predominately solved in interstitial lattice sites, discrete stress relaxation (DSR) events were detected, after which the film continued to behave in a linear elastic manner. DSRs were interpreted by uncorrelated movement of pre-existing dislocations. Particularly in the case of films deposited at higher temperatures, in-plane tensile stress was found at very small H concentrations of less than 0.005 H/V. Upon further H uptake, this turned into compressive stress. However, this stress increase differed from theoretical predictions. This behavior is explained by the generation of superabundant vacancies. Dislocation emission and plastic deformation are linked to the formation of the hydride phase in the $V_{1-x}Fe_x$ films.

© 2013 Acta Materialia Inc. Published by Elsevier Ltd. All rights reserved.

Keywords: Acoustic emission; Hydrogen; Vanadium; Thin film; Defects

1. Introduction

Hydrogen (H) absorption in bulk metals usually causes volume expansion of typically $\sim 10\%$ [1]. Ideally, this volume expansion occurs in the x , y and z directions. For thin films fixed to rigid plane substrates, the constraint condition allows hydrogen-induced lattice expansion only

in the z (film normal) direction [2,3]. Thus, a compressive biaxial stress of several GPa is observed [4,5]. This compressive stress response in the H-solution regime has been well described via linear elasticity theory [4,5]. To date, the H-induced biaxial stress developments in various metallic films like Nb [5], Pd [6] and Y thin films [7] have shown good agreement with this theory, demonstrating a linear elastic expansion behavior with increasing hydrogen concentration. However, above the yield stress the films can relax via plastic deformation, accompanied by dislocation generation, and a smaller stress increase is measured. This was further verified by scanning tunneling microscopy [8,9]. In addition, deviations from this linear relationship might occur when hydrogen changes its local position in the lattice [10]. With increasing hydrogen

* Corresponding authors. Address: Physical Sciences and Engineering Division, King Abdullah University of Science and Technology (KAUST), Thuwal 23955-6900, Saudi Arabia. Tel.: +966 2 8084493; fax: +966 2 8020061 (R. Gemma). Institute of Material Physics, University of Göttingen, Friedrich-Hund-Platz 1, D-37077 Göttingen, Germany. Tel.: +49 551 39 5025; fax: +49 551 39 5012 (A. Pundt).

E-mail addresses: Ryota.Gemma@kaust.edu.sa (R. Gemma), apundt@ump.gwdg.de (A. Pundt).

concentration, the compressive stresses usually continue to increase. Stress can also partially be released by film buckling [11]; the film thereby detaches from the substrate. This happens above a certain critical stress, depending on the adhesion between the film and the substrate [11].

The solubility of hydrogen in bulk metals is described by Sieverts' law [12], such that the hydrogen concentration is proportional to square root of hydrogen pressure. Sieverts' law implements that hydrogen is ideally solved on regular interstitial lattice sites, being either of tetrahedral (T) or of octahedral (O) type. Deviations from this law in a pressure–composition isotherm (p – c – T) also manifest the solubility limit and the onset of hydride formation.

In case of thin film systems, generally, deviations from the Sieverts' type behavior are expected, as the microstructure significantly contributes to the H solubility. The H solubility in thin films often exceeds that of bulk systems [13]. Such excess solubility is ascribed to “H trapping” at dislocations, grain boundaries (GBs), surfaces and vacancies because hydrogen atoms preferentially accommodate at such open volume defects with tensile stress fields [13]. Therefore, such preferential segregation of hydrogen may cause a deviation from the Sieverts' relationship, even in the solid-solution regime.

The impacts of hydrogen on the plastic behavior of vanadium bulk have recently been demonstrated by nano-indentation and micropillar compression measurements, verifying an enhanced formation of dislocations by the presence of hydrogen [14–18]. However, defect–H interactions in vanadium thin films have not yet been addressed in detail.

In this contribution, we have studied the H-related elastic and plastic behavior of vanadium thin films of different film thickness, ranging from 10 to 400 nm. A small content of iron (2–8 at.%) was homogeneously added to the films. It will be shown that the stress response deviates from theoretical linear elastic theory predictions and directly shows the effects of hydrogen on the defect generation and distribution in the films. For defect analyses, the results of in situ stress measurements by substrate curvature measurements and electromotive force (EMF) were combined with the results of in situ X-ray diffraction (XRD) and in situ acoustic emission (AE) technique. Only the combined approach through these measurements allows tracing dislocation motion and defect generation in thin films incorporated with hydrogen absorption behavior.

2. Experimental

2.1. Sample preparation and characterization

$V_{1-x}Fe_x$ ($x = 0.02$ – 0.08) films with thickness of 10–400 nm were deposited on sapphire (11 $\bar{2}$ 0) substrates (30 mm \times 7 mm \times 0.2 mm) at 297 K by ion beam sputtering with Ar gas. As will be shown later, the small difference

in the Fe content did not clearly contribute to a variation of the results. Films subjected to AE measurement were deposited on smaller sapphire (11 $\bar{2}$ 0) substrates (10 mm \times 7 mm \times 0.2 mm). For the purpose of stress measurement, some films with 100 nm thickness were deposited also on sapphire (0001) substrates of a beam shape (30 mm \times 7 mm \times 0.2 mm) at temperatures between 297 K and 1073 K. The deposition was carried out at a background pressure of 1×10^{-8} Pa and an Ar pressure of 2×10^{-2} Pa. The major residual gas was H₂ in the deposition chamber. But since the standard molar Gibbs free energy change (ΔG^0) of the V–H solid solution is -12 kJ (mol H)⁻¹ [19], H solubility in V at 297 K and at 10^{-8} Pa is $\sim 10^{-5}$ H/V only, and thus any pre-charging of H is negligible. At 1073 K, the residual H₂ increased to $\sim 1 \times 10^{-5}$ Pa. But this still verifies that the corresponding hydrogen concentration c_H is negligible, being only $\sim 10^{-5}$ H/V at 1073 K. All of the films prepared were subsequently terminated by a Pd layer of ~ 20 nm thickness at room temperature. This Pd overlayer promotes hydrogen absorption and also protects the film from oxidation.

The microstructure, the initial strain state, the film texture and the film/substrate orientation relationship were characterized by XRD. Especially for mechanical stress evaluation (Eqs. (10) and (11)) it is important to know the film/substrate orientation relationship. Scans were carried out with an X'pert MRD diffractometer (PANalytical, Co K α). In addition to normal 2θ – ω scans, rocking curves were recorded to confirm the mosaicity of the films. Subsequently, each film was subjected to hydrogen absorption experiments in an electrochemical cell designed for in situ stress and in situ AE measurement, respectively.

For some films, in situ XRD measurements at HASY-LAB, DESY (B2 beamline) have been employed to investigate lattice expansion while hydrogen loading is carried out.

2.2. Hydrogen loading and in situ XRD

Step-wise hydrogen loading was carried out galvanostatically at room temperature using a mixed solution of phosphoric acid and glycerin (1:2 in volume) as the electrolyte. An Ag/AgCl_{sat} electrode and a Pt wire were used as the reference and the counter electrode, respectively. For thin films systems, an electrochemical H-loading method is advantageous since c_H is controlled precisely and the chemical potential of hydrogen μ_H can be simultaneously monitored by measuring the EMF [20]. To convert EMF values into hydrogen pressures, the Nernst equation was used with a reference potential of the Ag/AgCl_{sat} electrode of -0.197 V against a standard hydrogen electrode, at 298 K. For bulk metal–hydrogen (M–H) systems, the result of the EMF measurement is assumed to be equivalent to a pressure–composition isotherm (p – c – T). In this study, this assumption was applied for thin film–hydrogen systems as well. According to Nernst equation, Sieverts' law is

expressed via the slope of RT/F in the EMF curves, where R is the gas constant, T is temperature and F is the Faraday constant [20].

Sieverts' law is expressed with Sieverts' constant K as follows:

$$c_{\text{H}} = K \cdot \sqrt{p_{\text{H}_2}} = \exp\left(\frac{\Delta G^0}{RT}\right) \cdot \sqrt{p_{\text{H}_2}} \quad (1)$$

where p_{H_2} is hydrogen pressure and R and T have their usual meaning. Under standard conditions, the ΔG^0 is related to the standard EMF E^0 as follows [21]:

$$\Delta G^0 = -nE^0F \quad (2)$$

Thus Eq. (1) gives

$$\ln c_{\text{H}} = \frac{-nE^0F}{2RT} \ln p_{\text{H}_2} \quad (3)$$

Here, E^0 is given by the measured potential E and reference potential E_{ref} as follows:

$$E^0 = E - E_{\text{ref}} \quad (4)$$

By considering standard condition $p_{\text{H}_2} = 1$ atm and the number of electrons in the reaction, $n = 2$ in Eq. (3), the following Nernst equation is given:

$$E = E_{\text{ref}} - \frac{RT}{F} \ln c_{\text{H}} \quad (5)$$

Thus, the constant RT/F thermodynamically relates to the Sieverts constant and describes ideal hydrogen solubility. Similarly, the measured EMF is converted to p_{H_2} [22].

With this electrochemical hydrogen loading method, in situ XRD was carried out at the HASYLAB B2 beamline in DESY with X-ray wavelength of 0.119 nm. Details of the cell design for these measurements can be found in Ref. [23].

2.3. In situ stress measurement

During the stepwise electrochemical hydrogen loading, the stress development in the film was monitored by recording the substrate bending. Details of this method and the setup have been published elsewhere [11]. According to the calibration of the sensor used in this study, the linear sensibility τ was $7.6 \text{ mV } \mu\text{m}^{-1}$ when Pd is used as a back plate, which works as an indicator of the distance to the sensor. The hydrogen absorption usually causes in-plane compressive stress in the film and the entire sample bends downwards, which shortens the sample–sensor distance z . This change, Δz , is detected as a change of capacitance ΔU and is given by

$$\Delta z = \frac{\Delta U}{\tau} \quad (6)$$

In the case of small bending, deflection of the substrate can be approximated with a triangular geometry. The change of curvature radius ΔR is therefore calculated from Δz and the length of the sample L [24]:

$$\Delta R \approx \frac{L^2}{2\Delta z} \quad (7)$$

From the change of curvature radius obtained, the hydrogen-induced in-plane stress $\Delta\sigma$ in the film can be calculated by Stoney's formula [25]:

$$\Delta\sigma = \frac{E_s \cdot t_s^2}{6t_f(1-\nu_s)} \cdot \frac{1}{\Delta R} \quad (8)$$

Here, E_s is the Young's modulus of the substrate, ν_s is the Poisson's ratio of the substrate and t_s and t_f are the thickness of the substrate and the film, respectively. The stress values were calculated by using the elastic moduli of sapphire published in Ref. [26], where $E = 418.1$ GPa and $\nu = 0.226$ for (0001).

Hydrogen absorption occurs practically only in the V–Fe layer and that in the Pd capping layer is negligible. Thus, only the total thickness of the V–Fe layer was taken into consideration for t_f in this study.

2.4. Elastic strain and stress resulting from linear elastic theory

Linear elastic theory on films clamped to substrates allows the elastic strain $\varepsilon_{\text{total}}$ to be calculated. For a (110)-oriented body centered cubic (bcc) film it is expressed as follows [5,27]:

$$\begin{aligned} \varepsilon_{\text{total}} &= \varepsilon_{\text{H}} + \Delta\varepsilon_{\text{zz}} = \left(1 + \frac{C_{11} + 3C_{12} + 2C_{44}}{C_{11} + C_{12} + 2C_{44}}\right) \cdot \varepsilon_{\text{H}} \\ &= 0.135 \cdot c_{\text{H}} \end{aligned} \quad (9)$$

using the H-induced expansion coefficient of pure vanadium, $\varepsilon_{\text{H}} = 0.063c_{\text{H}}$ (H/V) [28] and the stiffness constants of bulk vanadium $C_{11} = 229$ GPa, $C_{12} = 119$ GPa, and $C_{44} = 43$ GPa [29]. Because of elastic anisotropy, the hydrogen-induced in-plane stress response of the (110)-oriented bcc lattice must be separately considered in $\langle 110 \rangle$ and $\langle 001 \rangle$ systems, as shown in the following equations [5,27]. The negative sign appearing in the equations below accounts for compressive stress.

$$\begin{aligned} \sigma_{1=[1\bar{1}0]}[\sigma/c_{\text{H}}] &= -4 \cdot \left(\frac{C_{44}(C_{11} + 2C_{12})}{C_{11} + C_{12} + 2C_{44}}\right) \cdot \varepsilon_{\text{H}} \\ &= -11.7 \text{ GPa} \end{aligned} \quad (10)$$

$$\begin{aligned} \sigma_{2=[001]}[\sigma/c_{\text{H}}] &= -\left(\frac{2C_{44}(C_{11} + 2C_{12}) + C_{11}^2 + C_{11}C_{12} - 2C_{12}^2}{C_{11} + C_{12} + 2C_{44}}\right) \\ &\quad \cdot \varepsilon_{\text{H}} \\ &= -13.3 \text{ GPa} \end{aligned} \quad (11)$$

When in-plane orientation in the bending direction is in $[110]$, the theoretical slope of stress development for the films on sapphire (110) theoretically is -11.7 GPa, as calculated by Eq. (10). Any contribution of the Fe additive on the elastic constants is neglected in this calculation. In the case of in-plane isotropy, the theoretical slope of stress here is given by Eq. (12) as the average of Eqs. (10) and (11).

$$\langle \sigma \rangle [\sigma / c_H] = \left(\frac{\sigma_{1=[1\bar{1}0]} + \sigma_{2=[001]}}{2} \right) = -12.5 \text{ GPa} \quad (12)$$

2.5. AE measurement

An AE technique is usually employed to investigate plastic deformation and fracture behavior of bulk systems [30–32]. AE is sensitive to detect collective dislocation processes, twinning and other massive deformation events like crack formation and propagation. Recently, we demonstrated the potential of the AE method for studying stress release in M–H thin films, i.e. by film buckling [33]. A detailed description on this method can be found in Ref. [33]. In the present paper, the technique is for the first time used to measure dislocation processes in M–H thin films.

A schematic illustration of the AE experiment setup is shown in Fig. 1. The in situ AE measurements were performed with a computer-controlled DAKEL-XEDO-3 AE system, which is based on the threshold level detection of AE. The threshold voltage for the AE count was set at 480 mV (full scale was ± 2.4 V). The signal sampling rate was set at 4 MHz. A piezoelectric sensor MST8S (3 mm diameter, a frequency band from 100 to 600 kHz) was attached to the backside of the substrate. For reducing the loss of signal energy, thin substrates of 0.2 mm thickness and silicone grease couplants were employed for better wave propagation. Only the film surface was immersed in the electrolyte to protect the sensor from corrosion. Hydrogen was loaded stepwise, as described in Section 2.2, and the EMF was recorded simultaneously. The recorded AE counts during each stepwise H loading time (several minutes) were later summed up against c_H to examine dislocation movement and nucleation.

3. Characterization by XRD

3.1. Films of different thickness deposited at 297 K

All of the $V_{0.98}Fe_{0.02}$ films deposited showed (110) preferential orientation irrespective of film thickness. The XRD

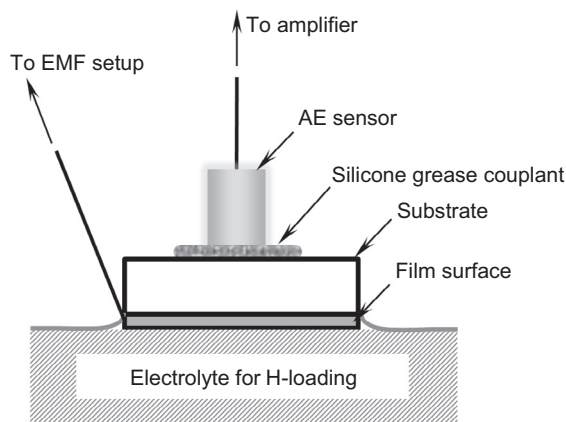


Fig. 1. Schematic drawing of in situ AE sensor placement for electrochemical hydrogen loading experiment (see text for details).

profiles of the as-deposited films of different thickness are summarized in Fig. 2a. These films were deposited at room temperature on (11 $\bar{2}$ 0) substrates. The films are under compressive in-plane stress, as can be seen by the (110) peak position shifted to smaller angles with respect to the bulk value. Results of texture measurements (not shown here) demonstrated in-plane, multi-domain orientations for these films. However, domains with $\langle 1\bar{1}0 \rangle$ direction close to the (0001) direction of the substrate are dominant. Thus, this anisotropic orientation relation is assumed as a first approximation, for the stress value calculations.

The initial compressive strain ε_0 can be calculated according to the out-of-plane lattice distance d , relative to the bulk reference value d_0 , by $\varepsilon_0 = (d - d_0)/d_0$. For the films with (110) orientation, the corresponding initial stress in $\langle 1\bar{1}0 \rangle$, as given by Eq. (10), is approximated by using Eq. (13)

$$\sigma_{0(1\bar{1}0)} = -4 \cdot \left(\frac{C_{44}(C_{11} + 2C_{12})}{C_{11} + C_{12} + 2C_{44}} \right) \cdot \varepsilon_0 \quad (13)$$

$$\sigma_{0(001)} = - \left(\frac{2C_{44}(C_{11} + 2C_{12}) + C_{11}^2 + C_{11}C_{12} - 2C_{12}^2}{C_{11} + C_{12} + 2C_{44}} \right) \cdot \varepsilon_0 \quad (14)$$

The resulting stress values as related to the peak positions in the XRD profiles are indicated in the upper axis of Fig. 2a, by utilizing d_0 in Ref. [34]. Irrespective of the film thickness, large compressive stresses of the order of GPa were found. This is often observed in the case of sputter-deposited films [35]. But, as a general trend, the peak shift is larger for the films with lower thicknesses. This trend means that the thinner V–Fe films conserve higher elastic energy, in the intrinsic state. The only exception from this trend is the 400 nm thick film. Table 1 summarizes X-ray crystallite sizes as estimated by Scherrer's formula, [36] and intrinsic in-plane stress of these films according to Eq. (13). Owing to the intrinsic stress which also causes widening of the peak width, the estimated crystallite sizes here are underestimated.

3.2. 100 nm Films deposited at different temperatures

In Fig. 2b, the XRD profiles and rocking scans of 100 nm thick films deposited on sapphire (0001) at different temperatures are shown as examples. The reference peak position of bulk $V_{0.92}Fe_{0.08}$ is also implemented, as calculated from the related lattice parameters in Ref. [34]. Out-of-plane (110)-orientation of the films was found regardless of deposition temperature between 297 and 1073 K. Clearly, the peak of the film deposited at 297 K is shifted to a lower angle compared to that of bulk. Thus, the film is under compressive stress. But the film deposited at 1073 K shows high-angle side shift, indicating an elastic deformation induced via the difference in thermal coefficient between the film and the substrate. The mosaic spread of 1.4° was found in the rocking scan profile of the film deposited at 297 K, while it decreases from 0.7° for the film deposited at 773 K, to 0.4° for the film deposited at 1073 K.

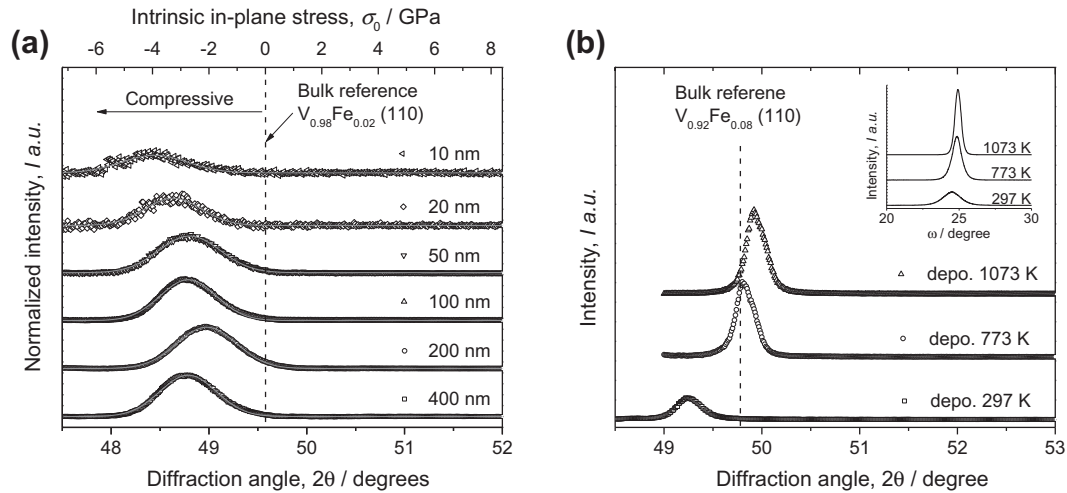


Fig. 2. XRD patterns of (a) $V_{0.98}Fe_{0.02}$ (110) films with thicknesses of 10–400 nm deposited on sapphire (11 $\bar{2}$ 0) substrates at room temperature, shown at normalized intensity scale and (b) $V_{0.92}Fe_{0.08}$ (110) films with 100 nm thickness deposited on sapphire (0001) substrates at 297 K, 773 K and 1073 K, respectively.

Table 1

X-ray crystallite sizes estimated by Scherrer's formula and intrinsic in-plane stresses of deposited films, as estimated by Eq. (13) and (14).

Film/substrate system	Deposition temperature (K)	Thickness, l (nm)	X-ray crystallite size, l (nm)	Intrinsic stress, σ_0 (GPa)
$V_{0.98}Fe_{0.02}$ (110)/Sapphire (11–20)	297	10 ± 3	12 ± 2	−3.92 ± 0.09
		20 ± 3	13 ± 1	−3.23 ± 0.03
		50 ± 1	13 ± 1	−2.57 ± 0.01
		100 ± 1	25 ± 1	−2.68 ± 0.01
		200 ± 2	16 ± 1	−1.99 ± 0.01
		400 ± 2	16 ± 1	−2.68 ± 0.01
$V_{0.92}Fe_{0.08}$ (110)/Sapphire (0001)	297	100 ± 1	37 ± 1	−1.42 ± 0.01
	773	100 ± 1	50 ± 1	0.06 ± 0.01
	1073	100 ± 1	51 ± 1	0.28 ± 0.01

Fig. 3 shows the pole figure of (a) $V_{0.92}Fe_{0.08}$ (110) deposited at 297 K and (b) the sapphire substrate (10 $\bar{1}$ 2). An epitaxial growth of (110) $-V_{0.92}Fe_{0.08}$ was established on (0001) sapphire, even at room temperature. Again, the pole figure of the film does not indicate growth of only one domain. Considering the three-fold symmetry of the substrate, at least three different domains with 60° in-plane rotation can be deduced, as shown in Fig. 3c. Fig. 3d shows the indexed substrate pole figure, for comparison. According to Figs. 2 and 3, the orientation relationship the films on (0001) sapphire is summarized as $V_{0.92}Fe_{0.08}$ (110)//sapphire (0001), $V_{0.92}Fe_{0.08}$ $\langle 001 \rangle$ //sapphire $\langle 10\bar{1}0 \rangle$. A similar epitaxy has been reported by Ikuhara [37].

As the three domains of the $V_{0.92}Fe_{0.08}$ (110) films grow with equal probability (Fig. 3a), the in-plane orientation of the film can be treated as isotropic, for the stress values calculation. By this assumption, the estimated intrinsic stress is given as an average of Eqs. (13) and (14). The estimated stresses and the crystallite sizes are also summarized in Table 1.

One should note that, regardless of the substrate orientation, there is large lattice misfit of $\sim 10\%$ between the film and sapphire substrate. This suggests that a considerable

number of misfit dislocations is present at the film/substrate interface, already at the as-deposited state. These intrinsic dislocations become relevant in the data interpretation later on.

4. Results and discussion

4.1. Stress development in films of different thickness upon hydrogen loading

The $V_{0.98}Fe_{0.02}$ films with thicknesses between 10 and 400 nm on sapphire (11 $\bar{2}$ 0) substrate were subjected to in situ stress measurement and hydrogen-induced stress and EMF was monitored simultaneously. The result of stress and EMF measurements for the films with thicknesses of 200 nm and 400 nm are summarized in Fig. 4. The straight dashed line along the stress curve represents this linear elastic prediction, according to Eq. (9). The straight dashed line in the EMF curves gives Sieverts' behavior with a slope of RT/F , according to Eq. (5). Corresponding EMF curves taken simultaneously are shown together.

Results for the film with 400 nm thickness are shown in Fig. 4a and b. With increasing c_H , the

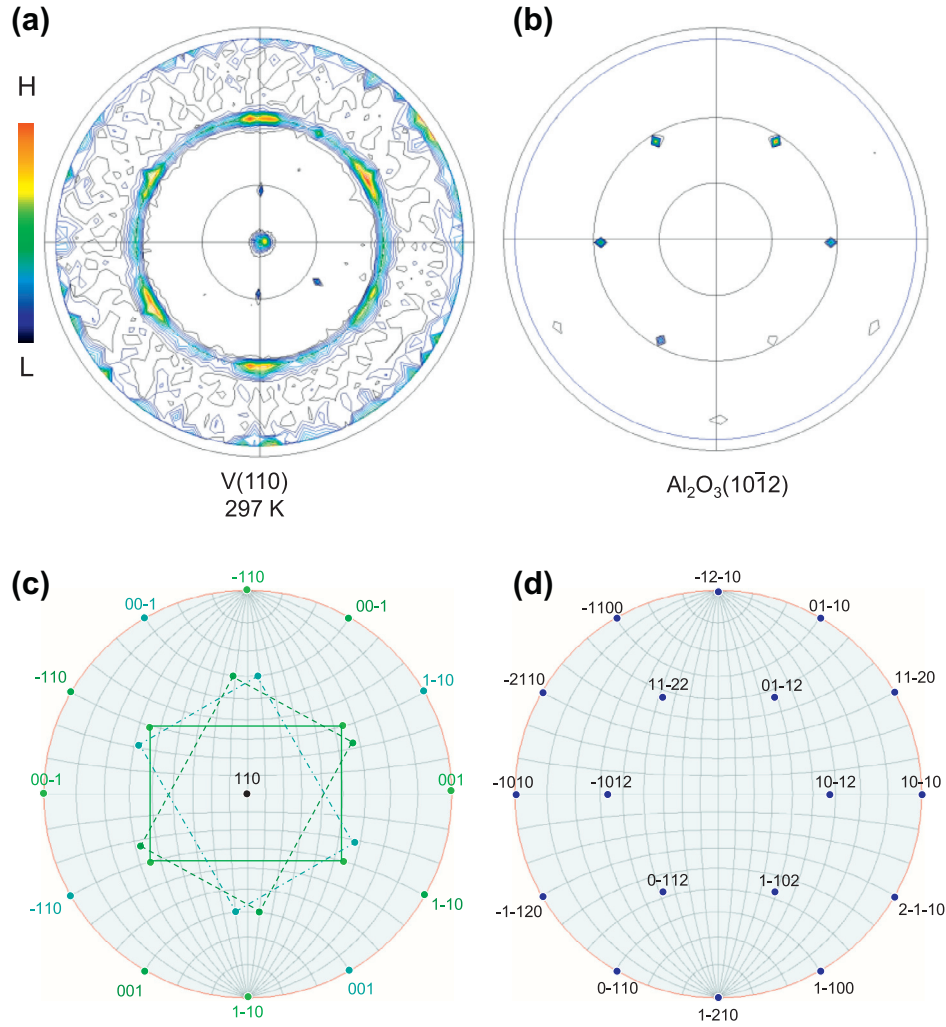


Fig. 3. Pole figures of (a) a $V_{0.92}Fe_{0.08}$ (110) film deposited at 297 K and (b) a sapphire substrate (10 $\bar{1}2$). Respective indices are shown in (c) and (d), suggesting three domains with $V_{0.92}Fe_{0.08}$ (110)//sapphire (0001), $V_{0.92}Fe_{0.08}$ (001)//sapphire $\langle 10\bar{1}0 \rangle$.

compressive stress (Fig. 4a) develops linearly with a slope of $\sigma/c_H = -11.2$ GPa, as indicated by the thick orange line. This is in accordance with the linear elastic prediction as drawn by the dashed line (Eq. (10), $\sigma'/c_H = -11.7$ GPa). In this region, the EMF curve (Fig. 4b) first lies below the slope of Sieverts' law (RT/F). This indicates that hydrogen is trapped at pre-existing defects such as dislocations up to around $c_H = 0.02$ H/V. Above this concentration, the EMF curve starts to obey Sieverts' law. This suggests that the majority of the hydrogen atoms are absorbed on interstitial lattice sites. With regard to the bulk phase diagram, these should be tetrahedral (T) sites [28,38] or distorted T sites [38] at this stage.

The EMF and the stress curves show a clear departure from the linear behavior, as indicated by σ_p , at similar concentration: at $c_H = 0.08$ H/V. In the EMF curve, such departure is regarded as the onset of a two-phase region of the sample and thus corresponds to the formation of the hydride where octahedral (O) sites are occupied. The α -solubility limit of the film is, therefore, $c_H^z = 0.08$ H/V.

Thus, the H solubility in the 400 nm V film is extended compared to that in bulk V $c_H^z = 0.03$ H/V [39–41].

In the stress curve, the measured deviation from the linear elastic behavior σ_p demonstrates elastic energy stress release in the film, e.g. by dislocation emission. As is shown later, this is in accordance with AE results, showing signals at this concentration. The onset of dislocation emission lies at around $c_H = 0.07$ – 0.09 H/V, which corresponds to the solubility limit. Dislocation emission, therefore, is caused by hydride formation, as reported elsewhere [8,42,43].

Further H uptake gives rise to relaxation of film stress and development of hydride phase until $c_H = 0.32$ – 0.35 H/V as indicated in Fig. 4. Above this concentration range, both the EMF value and the compressive stress start to increase again. Thereby, H atoms are further absorbed in the hydride phase and the H-induced compressive stress becomes considerable. The global features of the stress curve described above are in accordance with studies on Nb–H, Pd–H and Y–H thin films [6].

When the H-induced strain energy exceeds the adhesion energy between the film and the substrate, films detach

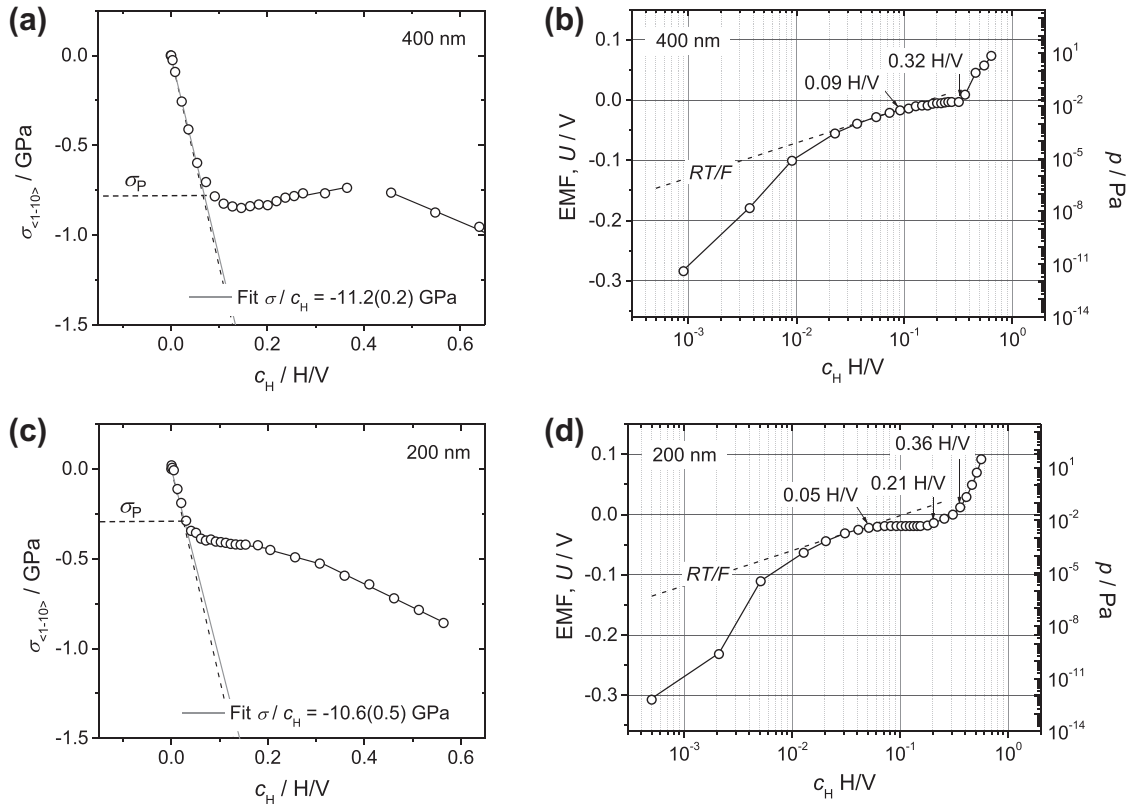


Fig. 4. H-induced stress curves and simultaneously recorded EMF curves of $V_{0.98}Fe_{0.02}$ films with thickness of (a, b) 400 nm and (c, d) 200 nm. Slope with dashed line demonstrates the linear elastic theory. Grayish straight line indicates fitting of the linear behavior. H-induced stress follows a linear elastic prediction. Dashed lines indicate large departure from this linear elastic behavior, as marked by σ_p .

from the substrates by forming “buckles” [11]. In this study, buckle formation occasionally occurred for films with thicknesses of 100–400 nm, when the concentration exceeds $c_H = 0.30$ – 0.40 H/V.

In bulk V–H, the two-phase region is located between 0.03 H/V and 0.45 H/V [39–41], yielding a gap width $\Delta = (0.45 - 0.03)$ H/V = 0.42 H/V. But the two-phase region of the 400 nm film lies between 0.07 H/V and 0.35 H/V, thus $\Delta = (0.35 - 0.07)$ H/V = 0.28 H/V, which is narrower than that of bulk V. Such a finding was also reported for Nb–H films [6,11], Nb/Ta–H multilayers [2], V–H films [19] or Pd–H nano-crystals [13,22,44]. Miscibility gap narrowing was attributed to the presence of GBs that do not participate in hydride formation and thereby change the hydriding volume fraction in the film [22], or that affect the individual grain’s solubility by strain energy [43]. Further, stresses arising between the film and the substrate also need to be considered to change thermodynamic equilibrium conditions, e.g. the width of the miscibility gap.

By trend, the results on the 200 nm film resemble that of the 400 nm film, as shown in Fig. 4c and d. Again, a good agreement with the theory is confirmed. At $c_H = 0.21$ H/V, the EMF curve increases continuously and then the curve bends upwards finally at $c_H = 0.30$ H/V. Such gentle change of the EMF curve in the plateau region is usually

not likely. But hydrogen and hydrogen-induced stress might cause this modification of the chemical potential of hydrogen, as suggested elsewhere [45–47]. The increase of the EMF in the plateau region suggests an increase of the compressive stress. In fact, this is consistent with the observation (see the range of c_H between 0.21 and 0.36 H/V in Fig. 4d).

Films that are thinner than 200 nm bring to light a new type of stress-release mechanism, arising in the low concentration range. Usually, linear elastic stress increase was reported for different films in this concentration range [5,6]. Results on 10–100 nm $V_{0.98}Fe_{0.02}$ films are summarized in Fig. 5a–d. Small discrete relaxation steps are clearly visible at low concentrations ($c_H < 0.10$ H/V) in the stress curves.

For example, up to $c_H = 0.04$ H/V the stress increase of the 100 nm thick film (Fig. 5a) follows the theory, Eq. (10). However, the curve discretely departs from the linear behavior at $c_H = 0.04$ H/V (guided by an arrow, indicated as σ_{DSR}). As shown by the corresponding EMF measurement (Fig. 5b), the Sieverts’ type solution of hydrogen on interstitial lattice sites begins at $c_H = 0.03$ H/V. This is almost the same concentration at which this small stress relaxation is observed (compare Fig. 5a and b). For convenience, we name it as “discrete stress relaxation” (DSR) and denote the onset stress of the DSR as σ_{DSR} .

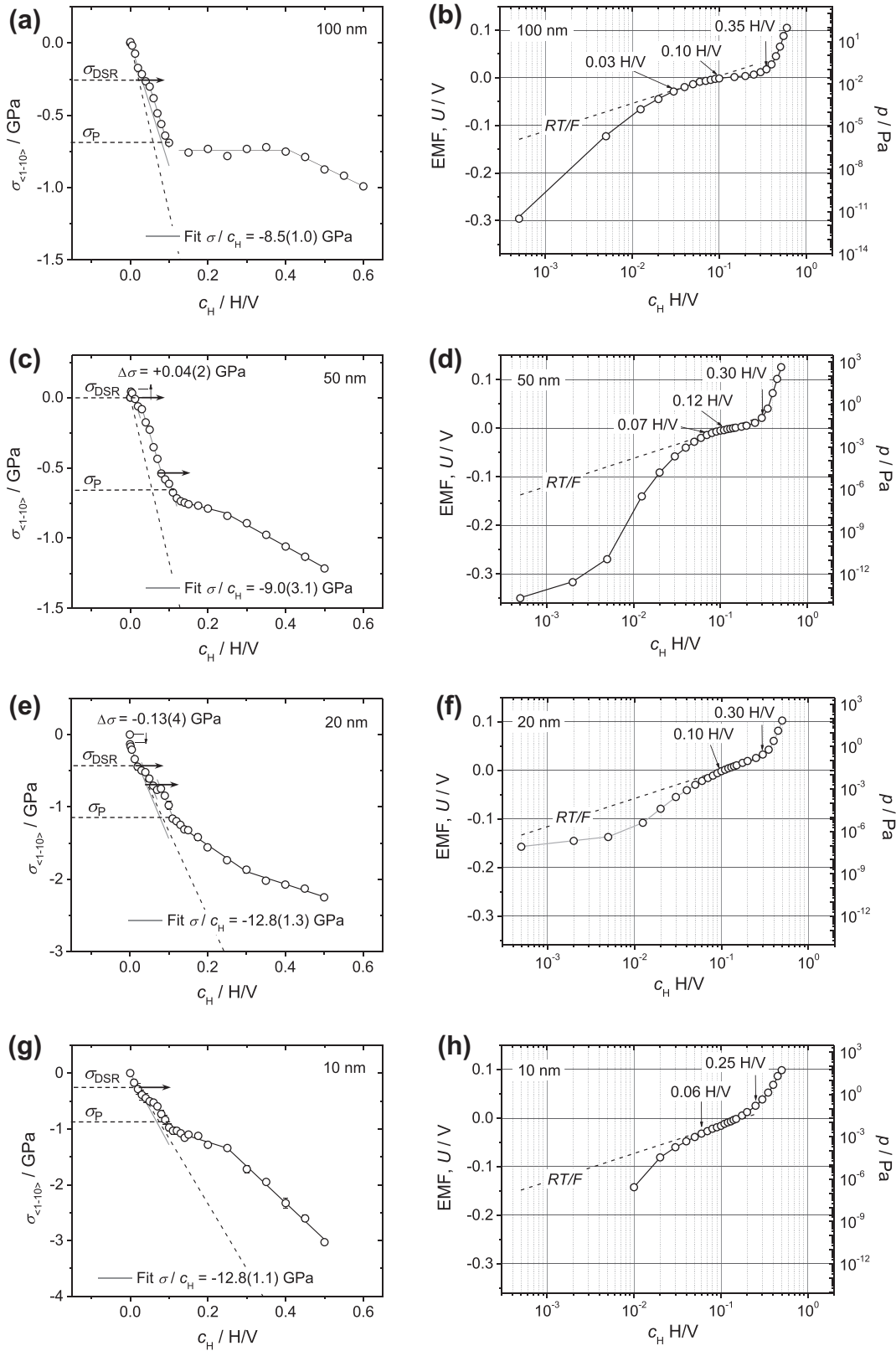


Fig. 5. H-induced stress curves and simultaneously recorded EMF curves of $V_{0.98}Fe_{0.02}$ films with thickness of (a, b) 100 nm, (c, d) 50 nm, (e, f) 20 nm and (g, h) 10 nm. Dashed line demonstrates the linear elastic theory. H-induced stress follows a linear elastic prediction. However, several small relaxations (σ_{DSR}) are also visible in the elastic regime, as indicated by arrows in the stress curves. Dashed lines indicate large departure from the linear elastic behavior, as marked by σ_P .

Upon further H uptake, the stress curve again follows the linear elastic prediction, up to $c_H = 0.10$ H/V. This recurrence of the linear elastic stress increase clearly differs from results reported on other M–H films. This behavior clearly differs from previously suggested plastic deformation of Nb films in the α -phase region [48].

At the concentrations above $c_H = 0.10$ H/V, a conventional behavior similar to that in Fig. 4 was observed. The end of this plateau region is in accordance with the end of the plateau in the stress curve at around $c_H = 0.40$ H/V. The entire curves are similar to those of thicker films.

The DSRs within the linear elastic regime become more pronounced for thinner film measurements. The 50 nm film shows two distinct relaxation steps at $c_H = 0.03$ H/V and at $c_H = 0.09$ H/V and subsequent recurrence to the linear elastic stress increase. Both events are marked with arrows.

Relaxation and departure from linear elastic stress increase occur at 0.12 H/V (Fig. 5c). The EMF curve of this film shows a considerably sloped plateau compared to that of the 100 nm film. Therefore, determining the concentration range that reveals Sieverts' type hydrogen solution on interstitial lattice sites becomes more difficult. It is suggested to range from 0.07 H/V to 0.12 H/V (Fig. 5d). Apart from this, there appears a small tensile stress $\Delta\sigma = +0.04(2)$ GPa at the very beginning of the stress curve, in Fig. 5c. Surprisingly, this implies tensile stress induced by hydrogen absorption in the film.

Fig. 5e and f shows the results on a 20 nm film. Again, DSRs appear in the linear elastic region, at 0.03(1) H/V and at 0.07(1) H/V, marked with arrows in Fig. 5e. They are even more clearly visible than in the results on the 50 nm film. The linear compressive stress development with a slope of $-12.8(1.3)$ GPa is in agreement with the theoretical slope of -11.7 GPa.

At concentrations above 0.13(2) H/V, both the stress and EMF curves show considerable steepness, implying larger H-induced in-plane stresses with thickness reduction.

Results on the thinnest film in the series, namely the 10 nm film (Fig. 5g and h) even more significantly show the above observations. DSR is visible, the final stress is maximum and the EMF curve's plateau is highly tilted.

To summarize, the results for the films with 10–100 nm thickness show a notable behavior of DSR events already in the elastic regime (see Fig. 5). These relaxation events are followed by a reappearance of the linear elastic stress increase. The lowest DSR stress, σ_{DSR} marks the onset of these events. At higher stresses, σ_p , a continuous relaxation i.e. departure from linear elastic stress increase, sets in.

Fig. 6 compares the lowest DSR stress, σ_{DSR}^t (half-filled circle) and relaxation stress σ_p^t (half-filled triangle) to literature data of the yield stress (open symbols), as measured for vanadium films of larger thickness by tensile tests [49,50]. The crystallite sizes t of Table 1 are applied, to allow for comparison with the literature data. The measured stress values σ_{DSR} , and σ_p have to be corrected by adding the intrinsic in-plane stresses of films, σ_0 , as determined from Fig. 2a: $\sigma_{DSR}^t = \sigma_0 + \sigma_{DSR}$, and $\sigma_p^t = \sigma_0 + \sigma_p$.

The dataset σ_p^t follows the linear trend of the reference data, and therefore qualitatively obeys the same scaling-law as the reference data. As this dependency is predicted for the yield stress of nanocrystalline materials, by the Hall–Petch relation, we relate σ_p^t to the yield stress. However, the dataset σ_{DSR}^t decays from the linear trend of the reference data, by showing a more reduced slope. This verifies the presence of a different type of process which occurs at stresses below the yield stress and which is initiated by the presence of hydrogen.

4.2. AE activity in films with different thicknesses

As reported in the last paragraph, a different relaxation behavior, the DSR, was found for films ≤ 100 nm (Fig. 5). Unfortunately, this thickness range cannot be analyzed by AE because the signal-to-noise ratio is too low. Therefore, in order to study the origin of the DSRs, the same type of film, only with a slightly larger thickness, was investigated by the in situ AE.

In Fig. 7a, the result of an in situ AE measurement on a 120 nm $V_{0.95}Fe_{0.05}$ film is shown. The thickness of the film is almost the same as in the case of the stress measurement. There was no AE count observed for $c_H < 0.039$ H/V (Fig. 7a, AE curve). This is well understood because hydrogen preferentially occupies open-volume defect sites. Here, plastic behavior is not expected (Stage I). The corresponding EMF curve verifies significant hydrogen trapping, especially at c_H below 0.0175 H/V. Above $c_H = 0.0175$ H/V, interstitial H occupation becomes remarkable (Fig. 7a, EMF curve), and as a consequence the compressive stress increases (Fig. 5a). At $c_H = 0.039$ H/V, which corresponds to the onset of

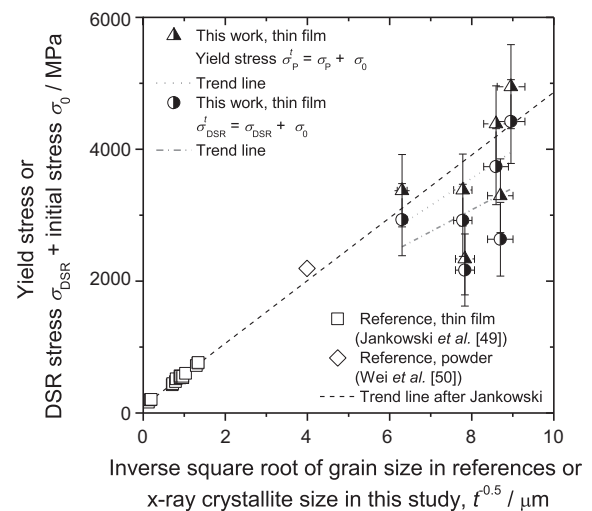


Fig. 6. Comparison of the total stress (initial stress $\sigma_0 +$ DSR stress σ_{DSR} , and initial stress $\sigma_0 +$ relaxation stress σ_p as regarded as yield stress) in the films of 10–100 nm with reported yield stress of vanadium films [49] and vanadium powder [50]. Error bar stems from different Fe content in the films (initial stress) and crystallite size. The stress scales with size. But smaller slopes of $\sigma_0 + \sigma_{DSR}$ and $\sigma_0 + \sigma_p$ than the extrapolation suggest possible impacts of hydrogen.

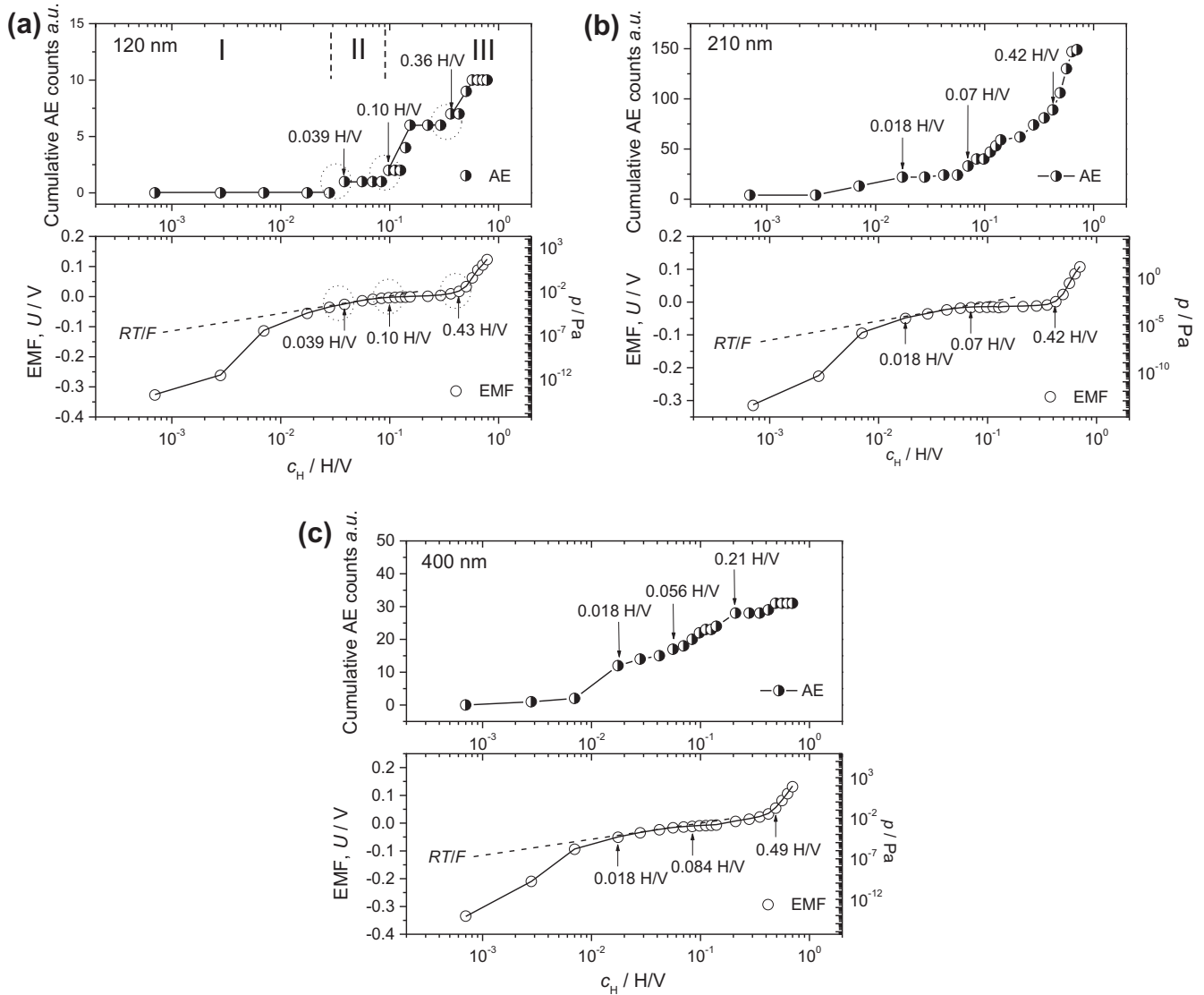


Fig. 7. In situ AE and simultaneously recorded EMF of $V_{0.98}Fe_{0.02}$ films with thickness of (a) 120 nm, (b) 210 nm and (c) 400 nm. Emission of new acoustic signal and corresponding concentration are indicated by arrows. Lines in the AE plots are drawn to guide the eyes. Note that the onset of first signal occurs at the onset of Sieverts' type behavior in the films.

Sieverts' law behavior, the first AE event was detected (Stage II). This first plastic process is consistent with the observed DSR at $c_H = 0.04$ H/V in Fig. 5a.

When the concentration reaches at $c_H = 0.10$ H/V, the AE events start to increase significantly. At the same concentration, the EMF curve shows a deviation from Sieverts' law. This indicates the onset of the two-phase field of this film (Stage III), where the hydride phase starts to form (Fig. 7a, EMF curve). The next inflection point of the cumulative AE curve is observed at $c_H = 0.36$ H/V. Here, the corresponding EMF curve still verifies the two-phase region. An inflection of the EMF is visible at a little higher concentration of $c_H = 0.43$ H/V. At this stage, film detachment also causes AE signals.

In Fig. 7b, results on a 210 nm film are shown. At $c_H = 0.018$ H/V, a distinct onset of AE is observed. No further signal is detected until the concentration reaches

$c_H = 0.07$ H/V, which is the onset of the two-phase field. A further increase of c_H causes an almost constant increase of the AE.

Results on a 400 nm film differ even from those of thinner films, as shown in Fig. 7c. In the case of this film, the correlation between slope changes in AE and EMF are not as pronounced as those for the two other films. At $c_H = 0.018$ H/V, an abrupt AE increase is detected (Fig. 7c). Thereafter, the AE shows a continuous increase.

As a global trend, the change of slope in the AE curve becomes more pronounced as the film thickness decreases (compare AE curves in Fig. 7a–c). For thicker films, AE events happen continuously in a wide c_H range. One should remember that the DSR in the low concentration range ($c_H < 0.07$ H/V) was not observed in the stress curve of films with $l \geq 200$ nm (see Fig. 4a and c). In fact, Nb–H thin films with 200 nm thickness for instance, do not show

any stress release in the α phase [5,6]. The results on the onset c_H of Sieverts' type behavior found in the EMF curves of in situ stress and AE measurements, and the onset c_H of the first AE, are compared in Table 2.

The general findings about the AE behavior of $V_{0.95}Fe_{0.05}$ single-layered films are summarized as follows:

- (i) AE increase at the onset of Sieverts' type behavior.
- (ii) AE increase at the deviation from Sieverts' type behavior.
- (iii) permanent AE signals for thicker films.

4.3. Combination of stress and AE results

The combination of the stress results of Section 4.1 and the AE results of Section 4.2 allows us to gain insights into the DSR events. As shown in Fig. 7a–c, at the onset of Sieverts' type behavior, meaning the concentration above which hydrogen is predominantly solved in interstitial sites in the V lattice, the first AE signal increase is initiated. As a reminder, the AE signal verifies any movement of dislocations. But as the stress measurements demonstrate, the elastic regime is not left yet at the corresponding concentration range (cf. Fig. 5a–d). Also, the Sieverts' type behavior demonstrates that hydrogen is solved in the lattice, and not at newly created defects. In combination, dislocation generation and multiplication are excluded in this regime. Therefore, we interpret the DSR events by an uncorrelated movement of pre-existing dislocations in the lattice. Pre-existing dislocations are present in the films, as according to the orientation relationship between the film and the substrate, a large misfit ($\sim 10\%$) is expected (see Fig. 3). A similar interpretation of AE events by a movement of pre-existing dislocations in Si was reported by Orlov et al. [51].

Fig. 6 demonstrates a decay of the σ'_{DSR} from the expected relation for the yield stress values, to a reduced slope. The yield stress gives the stress at which the material relaxes by dislocation generation and movement [52,53]. It obeys a scaling law, known as the Hall–Petch relation. The yield stress dependency, as expected from the scaling law, does not match the observed σ'_{DSR} data. This again demonstrates that both contributions, dislocation generation and movement, cannot be simultaneously involved here. All findings suggest an interpretation of the DSR with movement of pre-existing dislocations. The activation energy for relaxation via dislocations is reduced by the lack of

dislocation generation and the process can appear at a lower stress.

Further H uptake yields large departures from Sieverts' law at 0.10 H/V. Here, the film stress starts to relax and the AE curve shows a remarkable increase too. This behavior indicates that an “avalanche” of dislocations occurs at this concentration.

As Fig. 6 shows, the yield stress deduced from the Hall–Petch relation by extrapolating literature data on tensile tested V films almost matches σ'_p , the hydrogen-induced stress where stress release departs totally from linear elastic behavior. The EMF curves demonstrate that, at the related concentration, hydride formation sets in. It is well known from literature on hydrogen loaded bulk samples and films that hydride formation is often accompanied by the emission of extrinsic dislocation loops [8,42,43]. This supports the above interpretation of σ'_p as the yield stress of the films.

However, Barnoush et al. [54] reported that in the presence of H, the nucleation of a new dislocation loop occurs at a lower mechanical load than without H. They recorded this phenomenon by measuring the first “pop-in” in the load–displacement curve by nano-indentation, with and without hydrogen environment. Tal-Gutelmacher et al. [17] prove the same effect in V (100) single crystals. This effect is currently well understood by using the defect-acting-agent (“defactant”) model, proposed by Kirchheim [55]. The model ascribed the observed reduction of the “pop-in” load to a reduction of the dislocation line energy by H segregation. This effect is not seen here, since σ'_p obtained from hydrogen loaded V films follows the trend of the yield stress obtained for almost hydrogen-free V foils.

One should keep in mind that the reported nano-indentation studies were carried out by focusing on one large grain in bulk samples which contain an extremely low initial dislocation density [17]. Hardening effects by interference with pre-existing dislocations complicate the situation and, most possibly, make the defactant effect invisible. Therefore, a direct agreement of the stress obtained by nano-indentation with that of stress measurement of the films used in this study is not expected. However, one can speculate that the presence of hydrogen already enhances the movement of the pre-existing dislocations in the DSR events.

Up to now, the discussion does not take into account twinning deformation, known for bulk V [56]. This is due to a recent report that the twinning process in Ti–Al is

Table 2
Comparison of stress, EMF and AE results on the onset of Sieverts' type behavior and the onset of relaxation.

Thickness l (nm)	Onset c_H of Sieverts' type behavior, c_H (H/V)		Onset c_H of the first AE increase, c_H (H/V)
	EMF in stress measurement	EMF in AE	
$l = 100$ – 120	0.030	0.039	0.039
$l = 200$ – 210	0.022	0.018	0.018
$l = 400$	0.020	0.018	0.018

suppressed as the dimension of the specimen is decreased and plastic deformation by dislocations becomes dominant [57]. To finally confirm this for V, detailed microscopic observations are necessary, with a consideration of the reduction of the stacking fault energy under the presence of hydrogen [58,59].

4.4. Stress development depending on substrate orientation and deposition temperature

4.4.1. Stress dependence on substrate orientation

The results of 100 nm film on sapphire (0001) deposited at 297 K are shown in Fig. 8. After following the linear elastic behavior, a DSR is detected at $c_H = 0.04$ H/V (left figure, indicated by an arrow with σ_{DSR}). At the same concentration, the EMF curve starts to follow Sieverts' behavior (right figure). Above that concentration, the EMF curve further follows Sieverts' behavior until $c_H = 0.10$ H/V. In this regime, the stress curve again shows linear elastic behavior. At $c_H = 0.10$ H/V, the stress curve departs from the linear relationship. Simultaneously, the EMF curve shows a large departure from Sieverts' law. All the described features resemble the case of sapphire (11 $\bar{2}$ 0) described in Fig. 5a and b.

Obviously, the investigated films follow a general trend independent of the substrate orientation. Additionally, the small difference in the Fe content has a minor impact on the general trend (compare films of similar thickness).

4.4.2. Stress dependence on deposition temperature

However, films deposited at higher temperatures show a different behavior. Fig. 9 shows the stress dependency of a 100 nm film deposited on sapphire (0001) at 773 K (a) and that of a 100 nm film deposited at 1073 K (b), respectively. At low hydrogen concentrations, both films show tensile stress as indicated by $\Delta\sigma$. At 0.005 H/V, e.g. for the film deposited at 1073 K (b), the sign of the slope turns to minus, meaning that compressive stress appears. Some

traces of DSR are also visible. But, notably, the slope $\sigma/c_H = -7.6(7)$ GPa is rather smaller than that expected from the theory ($\sigma/c_H = -12.5$ GPa, Eq. (12)). Thus, the linear elastic theory alone might not explain these features.

4.5. Tensile stress caused by hydrogen

To unravel the curious behavior of this 100 nm film deposited at 1073 K (Fig. 9b) in the concentration range of 0–0.005 H/V, H-induced lattice expansion was investigated by in situ XRD and EMF time dependencies. The lattice expansion of a 100 nm $V_{0.92}Fe_{0.08}$ film is shown in Fig. 10, up to a concentration of 0.10 H/V. The experimentally determined expansions of the 100 nm film do not follow the one-dimensional expansion model. One should note here that there is no lattice expansion detected before the concentration reaches 0.005 H/V (see Fig. 10). This concentration range corresponds to the same concentration range where tensile stress was observed (cf. Fig. 9b).

In addition, clear differences are observed in EMF time dependencies. Slower transient behavior and lower EMF values are found for the films deposited at high temperatures, as shown in Fig. 11a. This reflects the “H trapping” region. These differences are not seen in the Sieverts regime (Fig. 11b), since the trapping effect is terminated here.

In order to elucidate the origin of the traps responsible for the findings in the low-concentration regime, impacts of different types of traps are discussed in the following [13,60]. GBs can act as trapping sites. Their fraction should be larger for the films deposited at 297 K compared to those deposited at higher temperatures (see rocking scans in Fig. 2b). Therefore, their impact is expected to be larger for the film deposited at 297 K. This is against the experimental finding where the films deposited at high temperatures show the largest effect. Therefore, GBs can be excluded as traps responsible for the low-concentration behavior of the V films. Dislocation generation can also be excluded because the AE measurements do not show acoustic events in this lower concentration range (compare Fig. 7a). Pre-existing dislocation density is calculated to be 10^{12} cm $^{-2}$ for the film deposited at 294 K, while it is 10^9 cm $^{-2}$ for the film deposited at 1073 K [61]. Therefore, the same consideration as for GBs is valid and thus disregarded. It is known that the binding energy of H at a vacancy is several hundred meV larger than that of hydrogen to an interstitial site [62]. Thus, in general, H trapping at vacancies can result in lower EMF values compared to classical Sieverts behavior. Since the area surrounded by the Sieverts solubility line and the EMF curve relates to the amount of traps [20], this suggests a higher vacancy concentration for the films deposited at higher temperatures.

This trapping effect at vacancies, however, cannot solely explain our results. The upper limit of thermal mono-vacancy concentration in the films is estimated by statistical thermodynamics [63,64]. Regarding the vacancy in bulk vanadium, the maximum mono-vacancy concentration is $c_{Vac} = 5.6 \times 10^{-9}$ Vac/V, by considering the deposition

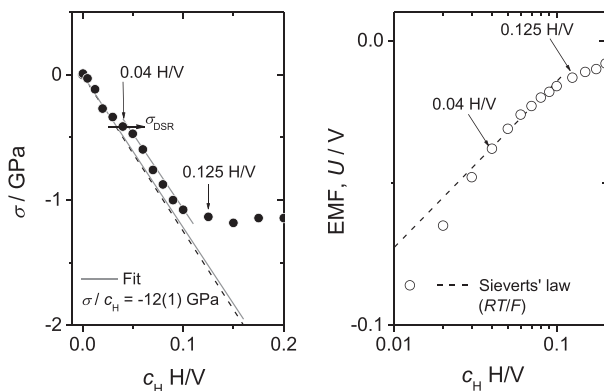


Fig. 8. H-induced stress curve and simultaneously recorded EMF curve of $V_{0.92}Fe_{0.08}$ film on sapphire (0001) with thickness of 100 nm, deposited at 297 K. The theoretical slope is shown by dashed line. The global trend is the same as the film deposited on (11 $\bar{2}$ 0), also showing DSR at 0.04 H/V, indicating minor impact of substrate orientation.

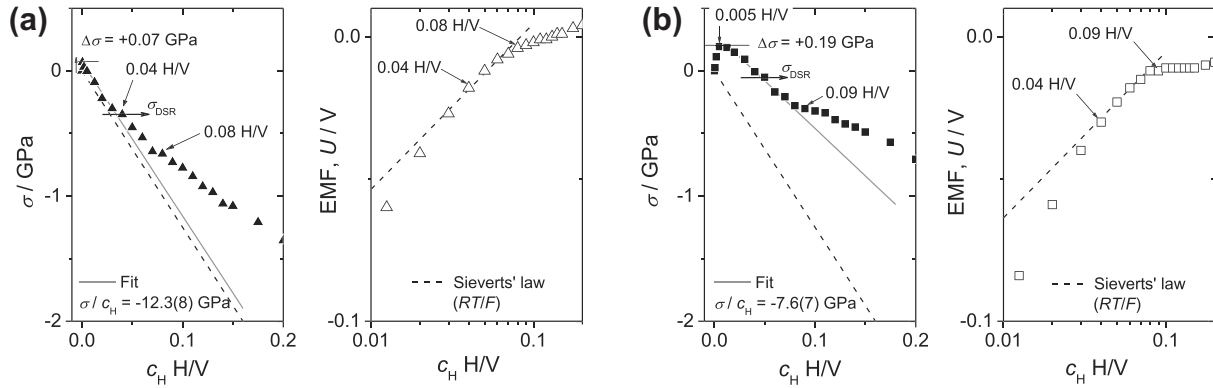


Fig. 9. H-induced stress curves and simultaneously recorded EMF curves of $V_{0.92}Fe_{0.08}$ film on sapphire (0001) with thickness of 100 nm, deposited at (a) 773 K, (b) 1073 K. DSR events are marked by arrows. Note the tensile stress recorded at small concentrations (until 0.005 H/V for the film of 1073 K). H-induced stress slope is smaller than that of theory marked as dashed line, especially in the case of (b).

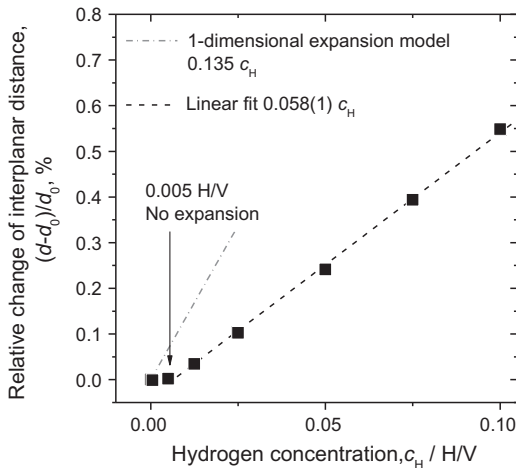


Fig. 10. Relative expansion of (110) in $V_{0.92}Fe_{0.08}$ film deposited on (1120) at 1073 K observed in situ XRD experiment. No expansion is recorded until $c_H = 0.005$ H/V. Experimental slope of expansion is smaller than the theoretical (one-dimensional) slope, consistent with the stress measurement of similar sample (Fig. 9b).

temperature of 1073 K and the formation enthalpy and entropy of a mono-vacancy in V, $\Delta H_V^f = 2.2$ eV and $\Delta S_V^f = 4.14 \times 10^{-4}$ eV K⁻¹, respectively [65]. If six H atoms are considered to be trapped in one vacancy at the

maximum [62,66], this results in a trapping concentration of $c_H = 3.36 \times 10^{-8}$ H/V. Obviously, this concentration is far too small to explain the trapping effects at concentrations of 0.005 H/V.

However, the observed behavior can be explained by hydrogen-induced vacancy formation. Vacancy formation can result in tensile stress in a clamped film when a Schottky pair is generated, meaning that the related metal atom goes to the film surface. The vacancy offers free volume and the surrounding metal lattice atoms tend to displace into the vacancy. In-plane displacements are suppressed by the clamping constraint. Thereby, the film gets into tensile stress. This is also expected to happen when hydrogen atoms are trapped to the vacancy until the trapping saturates.

In 1993, Fukai and Ōkuma [67] reported on the formation of superabundant vacancies (SAVs) in Pd and Ni bulk specimens under the presence of H, where the SAV concentrations (in at.%) were between 1 and several tens. They firstly observed SAVs at high temperature and high H₂ pressure conditions. The existence of SAVs has been confirmed in various systems [68–73]. In summary, these other experiments showed that a high fugacity of hydrogen results in SAV formation. Vacancy mobility is required, but high temperatures are not mandatory for SAV formation.

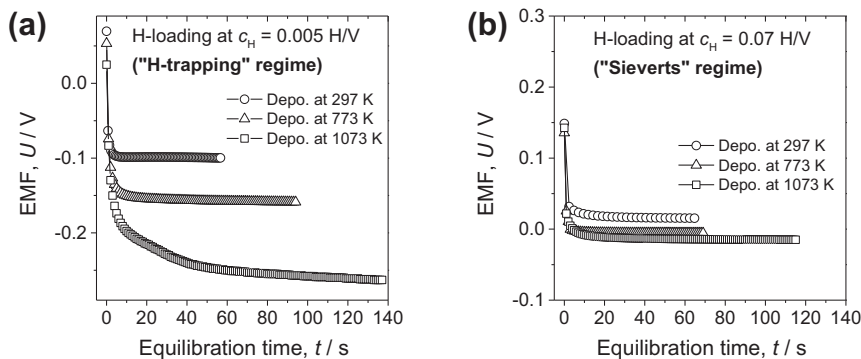


Fig. 11. EMF transient curves of $V_{0.92}Fe_{0.08}$ films deposited at 297–1073 K, recorded at (a) $c_H = 0.005$ H/V and at (b) $c_H = 0.07$ H/V. Slower kinetics and lower EMF values are seen for the films deposited at higher temperatures, marking a trace of H-trapping effect in (a). This kinetic difference is not clearly seen in (b) in Sieverts' regime. But the EMF of the film deposited at 1073 K keeps still lower value compared to the other films.

The expected lattice parameter change upon SAV formation can now be estimated. Following the concept of Simmons and Balluffi [74], the upper limit of the related relative lattice parameter contraction can be estimated by Eq. (15) [75]:

$$c_{\text{Vac}} = \frac{3 \frac{\Delta d}{a}}{v_{\text{Vac}}^R / \Omega} \quad (15)$$

where v_{Vac}^R is the relaxation volume around a vacancy and Ω is the atomic volume of the host metal. Fukai et al. have estimated the vacancy–H cluster concentration $c_{\text{Vac-H}}$ via Eq. (15). In Fukai's approach, it is assumed that the change of v_{Vac}^R caused by H trapping is negligibly small [76] and thus v_{Vac}^R is approximated as that of a Vac–H cluster, $v_{\text{Vac-H}}^R$. By this, the c_{Vac} in Eq. (15) gives a measure of $c_{\text{Vac-H}}$. For various bulk materials the value of v_{Vac}^R/Ω is ~ 0.2 – 0.3 [77,78]. This value is also assumed to be valid here. Therefore, the lattice contraction $\Delta d/a$ caused by a vacancy–H cluster $\varepsilon_0^{\text{Vac-H}} = \Delta d/a$ is given by Eq. (16):

$$\varepsilon_0^{\text{Vac-H}} = \frac{1}{3} \cdot \frac{v_{\text{Vac-H}}^R}{\Omega} \cdot c_{\text{Vac-H}} \quad (16)$$

To a first approximation, we follow the summary given by Korzhavii et al., taking $v_{\text{Vac}}^R/\Omega = 0.30$ [78] and thus $\varepsilon_0^{\text{Vac-H}} = -0.10 c_{\text{Vac-H}}$. This contraction accounts for free standing samples.

By considering constraint condition, we suggest a modification of Eq. (16) for thin film systems [79,80], for the case of a clamped film of cubic lattice structure. Similar to Eq. (9), the total out-of-plane lattice contraction in (110) caused by vacancies is as follows, giving almost twice as large a contraction than for the free standing case:

$$\begin{aligned} \frac{\Delta d_{(110)}}{d_{(110)}} &= -\varepsilon_{\text{total}} = -\varepsilon_0^{\text{Vac-H}} - \Delta \varepsilon_{zz} \\ &= -\left(1 + \frac{C_{11} + 3C_{12} + 2C_{44}}{C_{11} + C_{12} + 2C_{44}}\right) \cdot \varepsilon_0^{\text{Vac-H}} = -0.215 \cdot c_{\text{Vac-H}} \end{aligned} \quad (17)$$

By assuming Vac–6H complex, the expected $\Delta d/d$ by Eq. (17) gives $\Delta d/d = -2 \times 10^{-4}$ at $c_{\text{H}} = 0.005$ H/V. A similar approach is reported by Gruber et al. [80] on in situ monitoring of vacancy annihilation.

However, in our case, this contraction was not observed experimentally. This is probably due to the presence of a Pd capping layer deposited on the V layer, thereby V atoms are not able to move to the surface when interstitial-vacancies pairs are formed. Eventually, the pushed out atoms should accommodate rather at GBs, which may cause a weak in-plane compressive stress and corresponding out-of-plane lattice expansion. Consequently, both these counteracting responses might have canceled out each other.

Nevertheless, a clear trace of the SAV formation was detected in our stress measurement (Figs. 5 and 9). The stress associated to vacancy formation (Eq. (17)) is as follows by the same treatment as Eqs. (10)–(12):

$$\begin{aligned} \sigma_{[1\bar{1}0]}[\sigma/c_{\text{Vac-H}}] &= 4 \cdot \left(\frac{C_{44}(C_{11} + 2C_{12})}{C_{11} + C_{12} + 2C_{44}}\right) \cdot \varepsilon_0^{\text{Vac-H}} \\ &= 39.79 \text{ GPa} \end{aligned} \quad (18)$$

$$\begin{aligned} \sigma_{[001]}[\sigma/c_{\text{Vac-H}}] &= \left(\frac{2C_{44}(C_{11} + 2C_{12}) + C_{11}^2 + C_{11}C_{12} - 2C_{12}^2}{C_{11} + C_{12} + 2C_{44}}\right) \\ &\cdot \varepsilon_0^{\text{Vac-H}} = 45.34 \text{ GPa} \end{aligned} \quad (19)$$

$$\langle \sigma_{\text{Vac-H}} \rangle [\sigma/c_{\text{Vac-H}}] = \left(\frac{\sigma_{[1\bar{1}0]} + \sigma_{[001]}}{2}\right) = 42.57 \text{ GPa} \quad (20)$$

Positive stresses mean that the stress arising from SAV formation is tensile. Eq. (20) holds for ideally clamped films with isotropic in-plane orientation.

It is now possible to estimate vacancy–H complex concentration from the stress measurement results. From Eqs. (12) and (20), the in-plane stress induced both by hydrogen absorption and by vacancy–H complex formation is given by Eq. (21). Here, we consider total stress induced by H and vacancy, σ_{Total} , as a function of $c_{\text{Total}} = c_{\text{H}} + c_{\text{Vac-H}}$:

$$\sigma_{\text{Total}}[\sigma/c_{\text{Total}}] = -12.5 \cdot c_{\text{H}} + 42.57 \cdot c_{\text{Vac-H}} \quad (21)$$

By this, the H-induced vacancy concentration $c_{\text{Vac-H}}$ is estimated from the experimentally measured stress values by assuming 100% trapping probability. It should be noted here that the accommodation of atoms at GBs causes compressive stresses as well, and therefore Eq. (21) might somewhat underestimate the vacancy–H concentration.

It has been already confirmed that the H trapping almost terminates at $c_{\text{H}} = 0.04$ H/V (Fig. 9b). Above this concentration, possible impact of DSR gives rise to false $c_{\text{Vac-H}}$ and cannot be disregarded. Thus, the behaviors within $c_{\text{H}} = 0$ – 0.04 H/V are worth investigating for vacancy formation.

The result is shown in Fig. 12 as $c_{\text{Vac-H}}$ vs. c_{H} curves for the films deposited at different temperatures. The film deposited at 1073 K clearly shows a continuous increase of vacancy concentration. Starting with a slope of $c_{\text{H}}/c_{\text{Vac-H}} \sim 1$ until 0.005 H/V, the $c_{\text{Vac-H}}$ increase follows a slope of $c_{\text{H}}/c_{\text{Vac-H}} = 6.3(7)$ until c_{H} reaches 0.04. The calculated vacancy concentration marks 1 at.%, which is way above the thermal equilibrium concentration of 10^{-35} in pure bulk vanadium at room temperature. Theoretical calculations [62,66] show that the maximum H-trapping number at a mono-vacancy is 6 and further trapping results in even more positive energy than that of interstitial absorption. In spite of a crude estimation attempted here, the observed maximum $c_{\text{H}}/c_{\text{Vac-H}}$ ratio ~ 6 is in good agreement with theoretical prediction.

The vacancy migration energy in vanadium is ~ 1.2 eV [65], yielding the mobility of vacancy as only 1×10^{-3} nm s $^{-1}$ at 294 K. This mobility cannot immediately explain the high concentration of SAV in the V films. Therefore, it is reasonable to consider that the SAV concentration can be high near at the Pd capping side. Hydrogen, therefore, must affect both the formation energy and the mobility

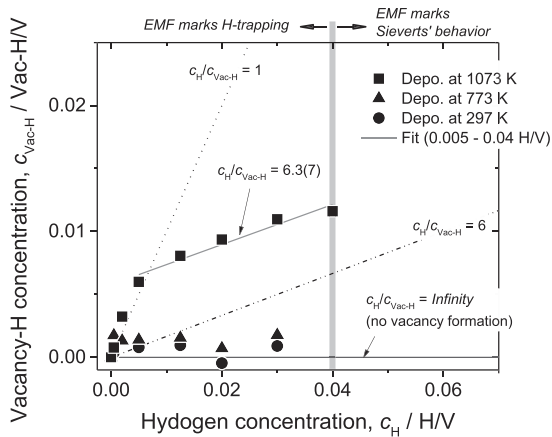


Fig. 12. Hydrogen-induced vacancy concentration in $V_{0.92}Fe_{0.08}$ film deposited on Al_2O_3 (0001) at 297 K, 773 K and 1073 K. The vacancy concentration was measured by in situ stress measurement (see Section 4.5). Inverse of the slope estimates number of H atoms coordinated at one monovacancy. In the film deposited at 1073 K, formation of 6H-Vac complex is suggested.

of vacancies. The impact of hydrogen on the defect formation energy was already implemented in the defectant concept of Kirchheim [55]. It is yet unclear why the film deposited at 1073 K clearly shows SAV formation whereas the other films do not. These films have larger crystallite sizes than the other films (Table 1). If we take into consideration the XRD result of the 1073 K film (Table 1), the out-of-plane lattice is contracted compared to bulk. The film deposited at 773 K shows a slightly similar trend (Table 1 and Fig. 12). Vacancies may be likely to be formed in such lattices that are contracted in the out-of-plane direction. Thus, the change of the intrinsic lattice constant in the out-of-plane direction might play a key role in SAV formation in thin films.

To summarize, introduction of SAVs may explain the observed tensile stress. We suggest that frozen-in thermal vacancies and continuous SAV formation might also contribute to the complex micro-structural development of the hydrogen loaded V films.

5. Conclusion

Hydrogen-induced elastic and plastic behavior of thin films of $V_{1-x}Fe_x$ ($x = 0.02-0.08$) with 10–400 nm thicknesses were studied by utilizing different in situ techniques. Besides the conventional metal film behavior upon hydrogen uptake, these films show remarkable new effects. Compressive in-plane stress development following the prediction from linear elastic theory ($-12.5 \text{ GPa}/c_H$) was observed upon H uptake in the in situ stress measurements. But additionally, DSRs were found for films of ≤ 100 nm, turning back to the elastic deformation regime upon further hydrogen uptake. Such H-induced DSRs in thin films have not been reported before. By careful examination of EMF curves and stress curves as well as in situ AE, DSRs are interpreted to be the result of uncorrelated movement

of pre-existing misfit dislocations. The DSR is commonly found at the onset of Sieverts' type behavior in the EMF curve, verifying the onset of hydrogen absorption in the interstitial sites. Concomitant in-plane stress becomes large at this point, especially for thinner films, driving the pre-existing misfit dislocations.

Films with larger crystallite size and contracted out-of-plane lattice constant (deposited at high temperatures) showed a remarkable tensile stress increase at very low concentrations (below 0.005 H/V), and a smaller stress slope than that predicted by theory at higher concentrations as well. The estimated hydrogen-induced vacancy concentration verified the Vac-6H complex theoretically predicted for the bulk material, and also for thin films. These trends were interpreted by the generation of hydrogen-induced SAVs influenced by the sample history.

The question remains open if the newly found features like DSRs or tensile stress attributed to SAVs appear only in V films or if they also occur in other thin metal films upon hydrogen absorption. Up to now, there are no reports. However, since the suggested origins are of a general nature, we suggest that other systems also show similar effects, maybe on a much smaller scale.

Acknowledgements

Financial support from the Deutsche Forschungsgemeinschaft via SFB 602 and PU131-9/1, the DESY and the Deutscher Akademischer Austauschdienst (DAAD) is gratefully acknowledged. J.C. acknowledges the Czech Science Foundation (Project P108/12/G043) for financial support. P.D. is grateful to the Charles University Research Center "Physics of Condensed Matter and Functional Materials" for financial support. R.G. would like to thank Talaat Al-Kassab at KAUST for financial support. We all gratefully acknowledge the availability of beamtime at HASYLAB B2 at DESY and Dmytro Trots for his technical support and reviewers for their valuable comments and suggestions.

References

- [1] Peisl H. In: Alefeld G, Völkl J, editors. Hydrogen in metals I. Topics in Applied Physics, vol. 28. Berlin: Springer Verlag; 1978.
- [2] Miceli PF, Zabel H, Dura JA, Flynn CP. *J Mater Res* 1991;6:964.
- [3] Rehm Ch, Fritzsche H, Maletta H, Klose F. *Phys Rev B* 1999;59:3142.
- [4] Yang QM, Schmitz G, Fähler S, Krebs HU, Kirchheim R. *Phys Rev B* 1996;54:9131.
- [5] Laudahn U, Fähler S, Krebs HU, Pundt A, Bicker M, v. Hülsen U, et al. *Appl Phys Lett* 1999;74:647.
- [6] Pundt A, Laudahn U, von Hülsen U, Geyer U, Kirchheim R, Wagner T, et al. *Mater Res Soc Symp Proc* 2000;594:75.
- [7] Dornheim M, Pundt A, Kirchheim R, v.d. Molen SJ, Kooij ES, Kerssemakers J, et al. *J Appl Phys* 2003;93:8958.
- [8] Pundt A, Getzlaff M, Bode M, Kirchheim R, Wiesendanger R. *Phys Rev B* 2000;61:9965.
- [9] Nörthemann K, Pundt A. *Phys Rev B* 2008;78:014105.
- [10] Pálsson GK, Wälde M, Amft M, Wu Y, Ahlberg M, Wolff M, et al. *Phys Rev B* 2012;85:195407.

- [11] Pundt A, Nikitin E, Pekarski P, Kirchheim R. *Acta Mater* 2004;52:1579.
- [12] Sieverts A. *Z Metall* 1929;21:37.
- [13] Pundt A, Kirchheim R. *Annu Rev Mater Res* 2006;36:555.
- [14] Nibur KA, Bahra DF, Somerday BP. *Acta Mater* 2006;54:2677.
- [15] Barnoush A, Vehoff H. *Corro Sci* 2008;50:259.
- [16] Mine Y, Doi K, Matsuoka S, Murakami Y. *J Soc Mater Sci Jpn* 2008; 57:255.
- [17] Tal-Gutelmacher E, Gemma R, Volkert CA, Kirchheim R. *Scr Mater* 2010;63:1032.
- [18] Deutges M, Knorr I, Borchers C, Volkert CA, Kirchheim R. *Scr Mater* 2013;68:71.
- [19] Papanthanasopoulos K, Wenzl H. *J Phys F-Met Phys* 1982;12:1369.
- [20] Kirchheim R. *Acta Metall* 1981;29:835.
- [21] Atkins PW, Clugston MJ. *Principles of physical chemistry*. London: Pitman; 1982.
- [22] Mütschele T, Kirchheim R. *Scripta Metall Mater* 1987;21:1101.
- [23] Dornheim M, Dissertation Universität Göttingen; 2002. p. 20. <<http://ediss.uni-goettingen.de/handle/11858/00-1735-0000-0006-B420-D>>.
- [24] Nikitin E. Dissertation Universität Göttingen; 2008. p. 115. <<http://ediss.uni-goettingen.de/handle/11858/00-1735-0000-0006-B47E-E>>.
- [25] Stoney GG. *Proc R Soc A* 1909;82:172.
- [26] Thokala R, Chaudhuri J. *Thin Solid Films* 1995;266:189.
- [27] Sander D. *Rep Prog Phys* 1999;62:809.
- [28] Magerl A, Berre B, Alefeld G. *Phys Stat Sol (a)* 1976;36:161.
- [29] Bolef DI. *J Appl Phys* 1961;32:100.
- [30] Siegel E. *Acta Metall* 1977;25:383.
- [31] Weiss J, Grasso JR. *J Phys Chem B* 1997;101:6113.
- [32] Chmelík F, Pink E, Król J, Balík J, Pešička J, Lukáč P. *Acta Mater* 1998;46:4435.
- [33] Cizek J, Procházka I, Vlach M, Zaludova N, Dobron P, Chmelik F, et al. *Procedia Eng* 2009;1:99.
- [34] Shiga M, Nakamura Y. *J Phys F: Met Phys* 1978;8:177.
- [35] Daniels BJ, Nix WD, Clemens BM. *Appl Phys Lett* 1995;66:2969.
- [36] Cullity BD. *Elements of X-ray diffraction*. 2nd ed. Reading, MA: Addison-Wesley; 1978.
- [37] Ikuhara Y. *Microsc Res Techniq* 1998;40:206.
- [38] Suzuki T. *Trans Jpn Inst Metals* 1985;26:601.
- [39] Maeland AJ. *J Phys Chem* 1964;68:2197.
- [40] Fukai Y, Kazama S. *Scr Metall* 1975;9:1073.
- [41] Schober T, Carl A. *Phys Stat Sol (a)* 1977;43:443.
- [42] Schober T. *Scr Metall* 1973;7:1119.
- [43] Makenas BJ, Birnbaum HK. *Acta Metall* 1980;28:979.
- [44] Weissmüller J, Lemier C. *Phys Rev Lett* 1999;82:213.
- [45] Wagner S, Pundt A. *Appl Phys Lett* 2008;92:051914.
- [46] Gonzalez-Silveira M, Gremaud R, Baldi A, Schreuders H, Dam B, Griessen R. *Int J Hydrogen Energy* 2010;35:6959.
- [47] Pivak Y, Schreuders H, Slaman M, Griessen R, Dam B. *Int J Hydrogen Energy* 2011;36:4056.
- [48] Laudahn U, Pundt A, Bicker M, v. Hülsen U, Geyer U, Wagner T, et al. *J Alloys Compd* 1999. p. 293–95, 490–94.
- [49] Jankowski AF, Go J, Jeffrey PH. *Surf Coat Tech* 2007;202:957.
- [50] Wei Q, Jiao T, Ramesh KT, Ma E. *Scr Mater* 2004;50:359.
- [51] Orlov AM, Skvovtsov AA, Frolov VA. *Tech Phys Lett* 1999;25:95.
- [52] Johnston WG, Gilman JJ. *J Appl Phys* 1959;30:129.
- [53] Mitchell TE, Foxall RA, Hirsch PB. *Phil Mag* 1963;8:1895.
- [54] Barnoush A, Bies C, Vehoff H. *J Mater Res* 2009;24:1105.
- [55] Kirchheim R. *Acta Mater* 2007;55:5129.
- [56] Westlake DG, Ockers ST. *J Less-Common Met* 1970;20:207.
- [57] Yu Q, Shan Z-W, Li J, Huang X, Xiao L, Sun J, et al. *Nature* 2010;463:335.
- [58] Windle RH, Smith GC. *Mater Sci J* 1968;2:187–91.
- [59] Oriani A. *Annu Rev Mater Sci* 1978;8:327.
- [60] Pundt A. *Adv Eng Mater* 2004;6:11.
- [61] Gemma R. Dissertation Universität Göttingen; 2011. p. 146. <<http://ediss.uni-goettingen.de/handle/11858/00-1735-0000-0006-B53B-7>>.
- [62] Ohsawa K, Eguchi K, Watanabe H, Yamaguchi M, Yagi M. *Phys Rev B* 2012;85:094102.
- [63] Seeger A, Schumacher D, Schilling W, Diehl J, editors. *Vacancies and interstitials in metals*. Amsterdam: North-Holland; 1970.
- [64] Haasen P. *Physical metallurgy*. Cambridge: Cambridge University Press; 1978. p. 220.
- [65] Janot C, George B, Delcroix P. *J Phys F: Met Phys* 1982;12:47.
- [66] Ouyang C, Lee YS. *Phys Rev B* 2011;83:045111.
- [67] Fukai Y, Okuma N. *J Jpn Appl Phys* 1993;32:L1256.
- [68] Fukai Y. *J Alloys Compd* 2003;356–357:263.
- [69] Fukai Y, Mizutani M, Yokota S, Kanazawa M, Miura Y, Watanabe YT. *J Alloys Compd* 2003;356–357:270.
- [70] Čížek J, Procházka I, Bečvář F, Kužel R, Cieslar M, Brauer G, et al. *Phys Rev B* 2004;69:224106.
- [71] Čížek J, Procházka I, Danis S, Cieslar M, Brauer G, Anwand W, et al. *J Alloys Compd* 2007;446–447:479.
- [72] Semiletov S, Baranova R, Khodyrev Y, Imamov R. *Kristallografiya* 1980;25:1162.
- [73] Krystian M, Setman D, Mingler B, Krexner G, Zehetbauer MJ. *Scr Mater* 2010;62:49.
- [74] Simmons RO, Balluffi RW. *Phys Rev* 1960;117:52.
- [75] Fukai Y, Ishii Y, Goto Y, Watanabe K. *J Alloys Compd* 2000;313:121.
- [76] Fukai Y. *The metal-hydrogen system*. 2nd ed. Berlin: Springer Verlag; 2005. p. 217.
- [77] Tucker CW, Sampson JB. *Acta Metall* 1954;2:433.
- [78] Korzhavyi PA, Abrikosov IA, Johansson B, Ruban AV, Skriver HL. *Phys Rev B* 1999;59:11693.
- [79] Botez CE, Elliot WC, Miceli PF. *Phys Rev B* 2002;66:075418.
- [80] Gruber W, Chakravarty S, Baetz C, Leitenberger W, Bruns M, Kobler A, et al. *Phys Rev Lett* 2011;107:265501.